Sound localization and quantification analysis of an automotive engine cooling module

Amoiridis, O.; Zarri, A.; Zamponi, R.; Pasco, Y.; Yakhina, G.; Christophe, J.; Moreau, S.; Schram, C.

DOI
10.1016/j.jsv.2021.116534

Publication date
2022

Document Version
Final published version

Published in
Journal of Sound and Vibration

Journal of Sound and Vibration 517 (2022) 116534

Contents lists available at ScienceDirect

Journal of Sound and Vibration

journal homepage: www.elsevier.com/locate/jsvi

Sound localization and quantification analysis of an automotive engine cooling module

O. Amoiridis [a], A. Zarri [a,*], R. Zamponi [b,a], Y. Pasco [c], G. Yakhina [c], J. Christophe [a], S. Moreau [c], C. Schram [a]

[a] von Karman Institute for Fluid Dynamics, Waterloosesteenweg 72, 1640 Sint-Genesius-Rode, Belgium
[b] Delft University of Technology, Kluyverweg 1, 2629 HS, Delft, The Netherlands
[c] Université de Sherbrooke, 2500 Boulevard de l'Université, Sherbrooke, QC J1K 2R1, Canada

ARTICLE INFO

Keywords:
Fan noise
Rotating beamforming
Sound-source localization
Automotive cooling module
Heat exchanger
Aeroacoustics

ABSTRACT

Sound emissions of an automotive engine cooling system are studied using both single-microphone directivity measurements and a rotating beamforming technique. These measurements provide reference acoustic data on such a system and some new understanding of the effect that the radiator induces on the distribution of sound sources. Indeed, the beamforming results indicate that, above the frequency limit allowed by the Rayleigh criterion, it is possible to localize and quantify the noise sources even through the heat-exchanger core. Moreover, for the investigated operating points along the fan performance curve, the sources are always distributed at the tip of the blades and, in particular, at the leading edge. The present evidence, confirmed by the similar trends of the frequency spectra with and without the heat exchanger, leads to the conclusion that the dominant sound mechanism is the turbulence-interaction noise. Nevertheless, this turbulence is produced within the gap between the fan ring and its casing rather than generated by the radiator core. The latter appears to induce negligible acoustic transmission losses but, more significantly, is found to have a minimal influence on the aerodynamic modification of sound sources for all the analyzed operating conditions.

1. Introduction

Aerodynamic noise emitted by low-speed axial fans has been receiving increasing attention in various industrial sectors. In modern automotive applications, the low-speed cooling fan has been identified as one of the major contributors to the total radiated sound field [1,2], especially for certain operating conditions such as, for instance, at traffic lights and in traffic jams, where the gear and wind noise are negligible. The axial fan is integrated into the engine cooling module and is placed downstream of a heat exchanger or radiator [3]. The whole automotive cooling module is installed in the under-hood compartment of the car. In such a complex system, several aerodynamic noise sources are present [4,5], as illustrated in Fig. 1. First, tonal contributions are generated by the periodic variation of the unsteady pressure load on the blades, which is caused by non-uniform inlet velocities or potential interactions with downstream obstacles. Secondly, the broadband sound is produced by several noise mechanisms, namely, turbulence-impingement noise, self-noise, and tip-leakage noise [6,7].

Turbulence-impingement noise, also denoted as leading-edge noise, is generated by the interaction of the incoming turbulence with the leading edges of the fan blades [5]. Hence, this noise mechanism is dominant in case of high turbulence intensity passing through the fan [8], but it can be negligible in case of clean inflow conditions [6]. Trailing-edge or self-noise is due to the sudden

* Corresponding author.
E-mail address: alessandro.zarri@vki.ac.be (A. Zarri).

https://doi.org/10.1016/j.jsv.2021.116534
Received 20 March 2021; Received in revised form 16 August 2021; Accepted 5 October 2021
Available online 22 October 2021

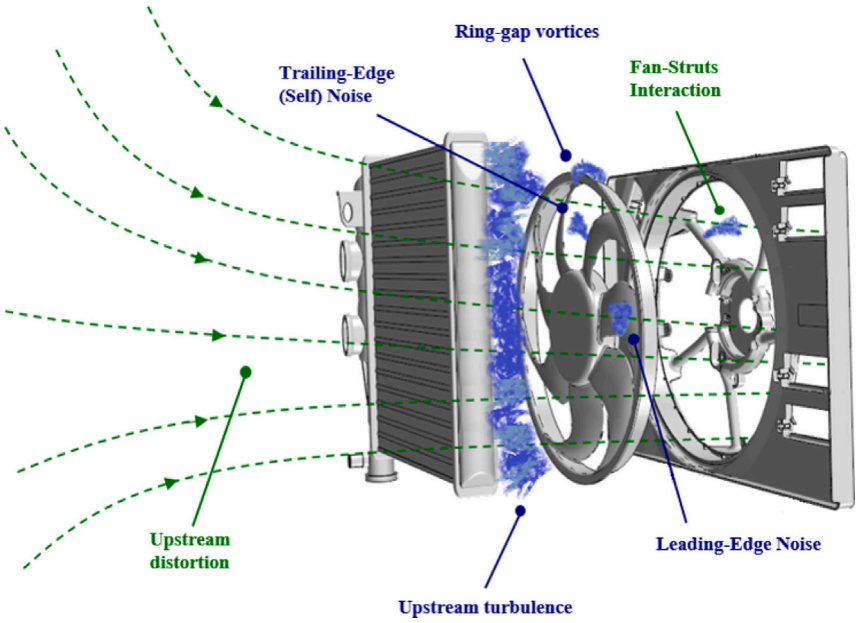

Fig. 1. Common noise mechanisms in automotive cooling modules: tonal mechanisms in green and broadband mechanisms in blue. (For interpretation of the references to color in this figure legend, the reader is referred to the web version of this article.)

distortion of the vortical structures born in the turbulent boundary layer with the blade trailing-edge discontinuity [9,10]. This noise still occurs even with clean inflow conditions since part of the boundary layer of such axial fans is always turbulent [11]. Tip-clearance or tip-leakage noise is produced by recirculating vortical structures that are formed due to the pressure difference between the pressure and suction sides in the tip region of the blades. Here, the recirculating flow can reach up to 6 % of the nominal flow rate [3], producing turbulence that interacts with the blade leading and trailing edges, increasing the low-to-mid frequency region of the noise spectrum [12,13]. It has been found that, in this region, the generated large vortices rotate at a slower speed than the rotor: the frequency of the impact is thus lower than the blade passing frequency (BPF), emitting subharmonic broadband or quasi-tonal noise [7]. Yet, most of the above studies consider the fan alone, flush-mounted on a plenum, and not installed in its cooling module [14,15]. Noise specifications that any automotive tier-one supplier has to fulfill are, however, in the latter configuration, which creates the need for reference experimental acoustic data and proper source localization in such a configuration.

Moreover, the effect of the presence of the radiator on the generation and propagation of fan sound sources under real application conditions is not yet fully characterized and understood. There is an aspect related to the absorption of the propagation of acoustic waves passing through the fine radiator core. In fact, Allam et al. [16] tried to exploit this in order to use the heat exchanger as a passive noise control tool, achieving a 5 dB reduction up to 2 kHz–3 kHz, but for a different plate heat-exchanger technology. Nevertheless, while highlighting the importance of considering the masking effect, Rynell et al. [17] concluded that, for the truck radiator they studied (similar technology as in the present study), the transmission loss effect was negligible compared to the change in the sound spectrum due to aerodynamic effects. In particular, the broadband sound components were found to be strongly correlated with the coherent turbulent structures in the flow, leading to a reduction of the sound emissions in the full-module case, especially at the BPF and harmonics. Christophe et al. [1] also studied generic locomotive cooling units with similar fins-and-louvers heat exchangers. They showed that the broadband spectrum is affected by the presence of the radiator, indicating the generation of turbulence through the radiator as the most likely cause. The aerodynamic effect induced by the radiator on the airflow at the fan inlet can have, in fact, several consequences on the dominant sound generation mechanisms. Another relevant study was conducted by Zenger et al. [18] in order to understand the effect that a highly distorted flow (they reached a turbulence intensity of up to 40 %) can have on the distribution of sound sources on two types of axial fans. In this case, turbulence grids were designed with the purpose of creating controlled distorted inflow conditions. The results showed that the sources have a tendency to distribute on the leading edge of the blade in case there is a strong turbulent interaction with the incoming flow. This has the effect of increasing broadband sound emissions, confirming the outcome of the previous study [19].

On the numerical side, full direct noise simulations of engine cooling modules have appeared with the Lattice Boltzmann methods (LBM) [14,15,20]. In such simulations of the actual experimental set-up, the heat-exchanger cores are modeled as equivalent inhomogeneous porous media, which prevent accounting for the possible acoustic diffraction or transmission loss of the cores. Yet, the excellent agreement of the computed noise levels and directivity with measurements in semi-anechoic chambers suggests that the automotive heat-exchanger cores are essentially acoustically transparent and transmission losses negligible. Compared with a fan-alone configuration, Lallier-Daniels [21] noticed, however, that the flow field of a fan in a duct or embedded in a module

flat shroud is significantly modified, particularly in the tip region [12]. Moreover, all these conclusions have been drawn at a single-module operating condition.

Therefore, an additional goal of the present study is to assess the effect that an actual radiator core can have on the sound emissions of an axial fan operated for different operating points. A microphone-array time-domain technique is used in the following work in order to achieve this objective. In addition, directivity measurements at various rotational speeds supplement the source localization and provide additional information about the nature of the noise source. Moreover, this study intends to provide a first clean database on an automotive engine cooling fan working in various configurations, tested in two different facilities.

In the work presented hereafter, Section 2 describes the fundamentals of the array-based acoustic source localization. Section 3 outlines the setups in which two complementary experimental campaigns in two different anechoic wind tunnels have been carried out to provide reference acoustical data in well-controlled environments. The single-microphone measurements, directivity measurements, and sound-localization maps for several configurations are outlined and discussed in Section 4. Finally, conclusions are drawn in Section 5.

2. Acoustic localization methodology

Microphone array methods can be employed in order to localize and quantify the frequency-dependent location and strength of sound sources at different operating points on various configurations. Conventional array-based measurement techniques have been widely used to characterize aeroacoustic sound sources in terms of strength and location on stationary objects. To apply these methods to axial fans, the motion of the fan relative to the microphone array and, thus, the Doppler effect, needs to be considered. Both time- and frequency-domain methods have been developed for this purpose.

Sijtsma et al. [22] approached this challenge by using a transfer function for a moving monopole source in uniform flow to reconstruct the signal in the time domain and develop an algorithm able to deal with rotating sources, named rotating source identifier (ROSI). They validated the method with rotating whistles and applied it to localize and characterize sound sources on a hovering helicopter rotor and on wind-turbine blades. The capability of this algorithm has been further examined by Oerlemans et al. [23] for the investigation of real-scale wind-turbine sound sources. In addition, Sijtsma [24] applied ROSI for the investigation of turbofan engine noise.

Pannert and Maier [25] compensated the motion in the frequency domain through the calculation of the cross-spectral matrix in the rotating frame of reference from stationary data. A constant fan speed is required to apply this method. A different approach is to arrange the microphones on a ring coaxial to the rotational axis of the fan. Then, the microphone data can be re-sampled to a virtual array, rotating together with the focus point [26,27]. This method is called virtual rotating array (VRA) and does not require a constant rotational speed. Zenger et al. [28] applied the VRA method to characterize the sources of an axial fan for different operating points, whereas Zenger et al. [18] tested the VRA algorithm in forward- and backward-skewed axial fans under distorted inflow conditions. An extension of the VRA technique exploiting arbitrary microphone configurations was recently presented by Jekosch and Sarradj [29], pointing out that the VRA method does not require a specifically-designed circular microphone array to investigate rotating sound sources.

An extensive comparison between VRA and ROSI algorithms has been conducted by Kotán et al. [30], highlighting the increased computational cost of ROSI against the VRA method. Nevertheless, both techniques accurately predict the location and the strength of the rotating source. The main advantage of VRA as a frequency-domain method is that deconvolution algorithms can be applied to improve the spatial resolution of the beamformer output. The ROSI method does not require the alignment between the center of the array and the center of rotation. This aspect turns out to be particularly useful in wind-tunnel experiments with limited space at disposal, as in the present case.

There have been studies on localizing sound sources on low-speed cooling fans that employed approaches in both time [31–34] and frequency domains [26,35,36]. Nevertheless, all these investigations focused on the fan-alone configuration without the presence of a suction-side radiator. Therefore, the coupling between the fan and the radiator is essential to evaluate the global emitted noise properly and gain further insight into the acoustic phenomena.

In the present work, the microphone array method described by Sijtsma et al. [22] is implemented in order to post-process the measured data. The algorithm has been validated through its application to two benchmark datasets featuring simulated rotating monopole sources [37]. A detailed description of the method can be found in [22], only a summary is presented hereafter. The ROSI method constitutes a beamforming algorithm in the time domain able to deal with rotating sources moving with subsonic speed. The beamforming results are calculated on a scanning grid (SG), which is an ensemble of potential sources rotating together with the sound sources of interest. If we assume a potential source located at the time-dependent position $\boldsymbol{\xi}(t)$ emitting a sound signal σ at time τ_e, the sound signal p will be received at the microphone location x at time t.

The wave equation for a moving monopole source in a stationary medium is then considered in order to determine the acoustic transfer function between the source signal σ and the measured pressure field p:

$$\frac{1}{c_0^2}\frac{\partial^2 p}{\partial t^2} - \nabla^2 p = \sigma(t)\delta(\boldsymbol{x} - \boldsymbol{\xi}(t)), \tag{1}$$

where c_0 is the speed of sound. The solution of Eq. (1) is found following the derivation described in the original work of Sijtsma et al. [22] and can be expressed as

$$p(\boldsymbol{x}, t) = \frac{-\sigma(\tau_e)}{4\pi\{c_0(t-\tau_e) + [\frac{-\boldsymbol{\xi}'(\tau_e)}{c_0}]\cdot[\boldsymbol{x} - \boldsymbol{\xi}(\tau_e)]\}}, \tag{2}$$

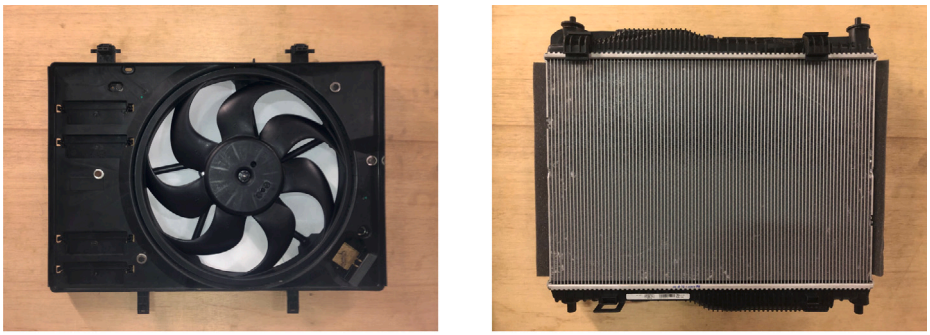

(a) (b)

Fig. 2. Automotive cooling module installed on the middle wall of the ALCOVES anechoic chamber: (a) fan alone -FA- configuration (b) full module -FM- configuration.

Hence, it follows that, for free-field conditions, the transfer function F from a moving source in $\boldsymbol{\xi}(t)$ to a receiver in $\boldsymbol{x}$, is given by

$$F(\boldsymbol{x}, \boldsymbol{\xi}(\tau_e), t, \tau_e) = \frac{p(\boldsymbol{x}, t)}{\sigma(\tau_e)} = \frac{-1}{4\pi\{c_0(t-\tau_e) + [\frac{-\boldsymbol{\xi}'(\tau_e)}{c_0}] \cdot [\boldsymbol{x} - \boldsymbol{\xi}(\tau_e)]\}}, \tag{3}$$

where $\boldsymbol{\xi}'(\tau_e)$ is the velocity of the moving source at the emission time, whereas the relation between the arrival time t and the emission time τ_e is given by

$$\Delta t = t - \tau_e = \frac{\|\boldsymbol{x} - \boldsymbol{\xi}(\tau_e)\|}{c_0}. \tag{4}$$

The arrival time vector $(\Delta t + \tau_e)$ at which the recorded pressure signals should be evaluated through Eq. (3) does not coincide with the time instants at which the measurement system samples the data. Hence, in order to obtain the proper values of the recorded pressure signals at the desired times, the measured signals are linearly interpolated. The amplitude variation is also taken into account by exploiting the transfer function of the potential source. Afterward, the interpolated pressure signals are evaluated at the original uniformly-spaced emission-time instants and de-Dopplerized [38,39]. The latter procedure allows to eliminate the Doppler effect from the measurements and is essential to identify moving sound sources correctly. Finally, the reconstructed signal is Fourier-transformed, and the resulting sound pressure level L_p for the investigated point of the SG is obtained. This routine is repeated for all the SG points such that the final source-distribution map can be determined. Hence, each individual sample is time-shifted and amplitude-adjusted depending on the position and speed of the source at the emission time in order to reconstruct the emitted signals from the measured ones.

3. Experimental campaigns and setups

The experimental work presented in the following sections took place in two laboratories: at the von Karman Institute for Fluid Dynamics (VKI) and at Université de Sherbrooke (UdeS). The experimental setups and campaigns at VKI and UdeS are hereafter described separately. Nevertheless, the studied engine cooling module is the same.

3.1. Engine cooling module

Experimental investigations are performed on two different samples of the same engine cooling module, designed by the automotive supplier-company Valeo at La Verrière, France. The geometry of the L-shaped ring fan, shown in Fig. 2(a), consists of 7 forward-skewed blades that are almost equally spaced and have a varying chord and stagger angle. The diameter of the fan is $d_{fan} = 380\,\text{mm}$, the hub-to-tip ratio is 0.37, whereas the gap size between the casing and the rotating ring is 6 mm [40]. The Reynolds number based on the chord at the tip of the blade is approximately 2.45×10^5, stating that the fan is working in the laminar–turbulent transition regime [41]. The Mach number at the blade tip, related to an operational rotational speed of 3400 rpm, is 0.19, and, thus, a subsonic incompressible regime can be considered.

As shown in Fig. 2(b), at VKI, the suction-side radiator is installed in the anechoic chamber by clipping it on the fan shroud displayed in Fig. 2(a). Differently, at UdeS, the cooling module is suspended, as detailed in Section 3.5. More details regarding the geometrical parameters characterizing the heat exchanger can be found in Table 1.

The rotational speed of the automotive fan is evaluated using a diode probe with a reflective aluminum tape fixed at the hub of the rotor. The beam emitted by the diode is reflected on the aluminum tape at each fan revolution. Therefore, this trigger per revolution signal is used to track the rotational speed of the fan over time. In addition, the diode signal is acquired synchronously with the microphone data allowing the computation of the angular position of the fan.

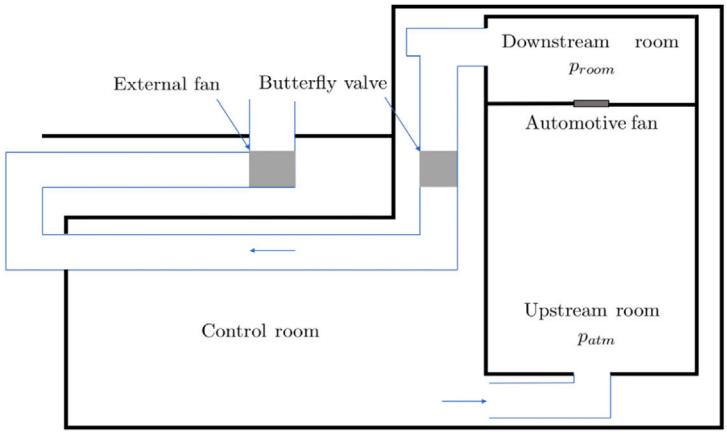

Fig. 3. ALCOVES anechoic chamber sketch adapted from Dominique et al. [43].

Table 1
Geometrical parameters of the heat exchanger.

Number of coolant pipes	92	Slat thickness	0.12 mm
Coolant pipe height	385 mm	Space between slats	2.5 mm
Coolant pipe depth	20 mm	Heat exchanger width	558 mm
Coolant pipe width	1.5 mm	Heat exchanger height	385 mm
Space between pipes	4.5 mm	Heat exchanger depth	20 mm

3.2. VKI ALCOVES anechoic laboratory

The VKI experimental measurements are carried out in the ALCOVES anechoic laboratory, where aerodynamic and aeroacoustic measurements can be conducted simultaneously. This testing facility is characterized by a cut-off frequency of 200 Hz [42] and composed of two anechoic rooms separated by a modular wall partition that can accommodate different components such as automotive cooling systems [40] and ducted fans [43]. The flow inside the wind tunnel is driven by an auxiliary fan placed in a downstream circuit, generating a pressure difference across the rooms. Acoustic treatments are included within the pipe in which the external fan is installed to prevent the propagation of the noise emissions upstream toward the test section. A detailed scheme of the anechoic chamber is illustrated in Fig. 3.

The test chambers are equipped with static sensors permitting the computation of the pressure difference ΔP generated across the partition wall. The airflow rate Q_m passing through the module is provided by the external auxiliary fan and is measured according to ISO 5167 [44].

3.3. VKI microphone array

The microphone array considered for the present study at VKI is a planar Dougherty array [45] with 64 microphones distributed over seven logarithmic arms and with a diameter of $D_a = 1.5$ m (see Fig. 7(b)). The antenna, shown in Fig. 4(b), is characterized by a light and easily transportable structure and is equipped with inexpensive capacitor-based Knowles electrets (model FG-23329-P07 with a frequency response ± 3 dB and a frequency range of 100 Hz to 10 kHz). The microphone array is installed at a distance of $d_{a-ss} \simeq 2.5\, d_{fan}$, perpendicular to the rotation axis of the fan, on the suction side, as depicted in Fig. 4(a). With the present setup, the minimum resolvable source separation is given by the Rayleigh criterion [46] as

$$R \simeq d_{a-ss} \tan\left(\frac{1.22\, c_0}{f\, D_a}\right), \tag{5}$$

where c_0 is the speed of sound and f is the investigated frequency.

In addition, the calculation of the coordinates of the center of rotation is performed by applying a conventional beamforming method [47] to the acoustic data generated by a loudspeaker installed at the center of the fan and emitting a white-noise signal, as also done in [48]. The position of the monopolar source obtained and displayed in the sound map is taken into account to translate the scanning grid, making it possible for the algorithm to follow the movement of the sources rotating together with the fan. Finally, the processing parameters considered to process the experimental data are indicated in Table 2.

3.4. VKI performance curves

At VKI, the automotive cooling module is investigated for two configurations: fan alone (FA) and full module (FM). For each of these, three different operating points (OP) are chosen, as shown in Fig. 5(a).

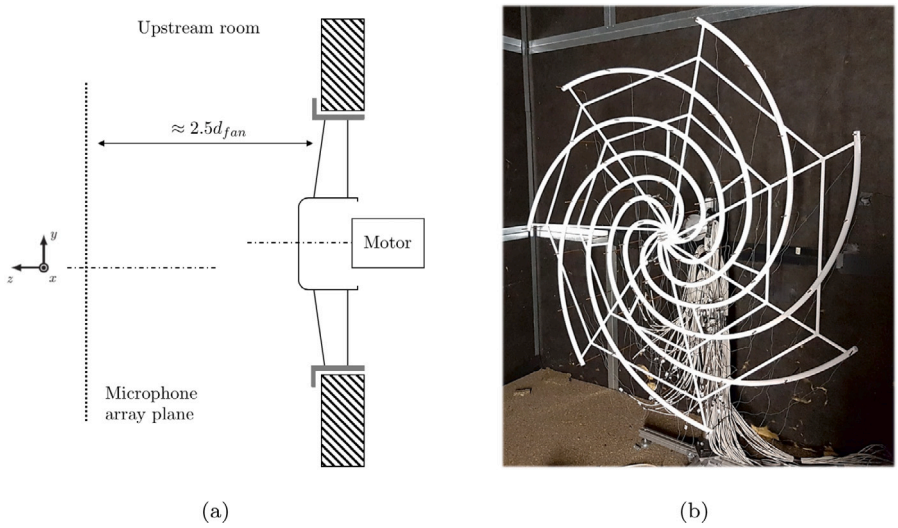

Fig. 4. (a) Position of the microphone array in the ALCOVES upstream room with respect to the axial fan. (b) 64-microphones Dougherty array employed for the campaign.

Table 2
Data-processing parameters of the experimental test case.

Measurement time	5 s	Grid translation	$(x, y) = (0.09\,\text{m}, 0.18\,\text{m})$
Sampling frequency	51.2 kHz	Rectangular grid	$x = \pm 0.25\,\text{m},\ y = \pm 0.25\,\text{m}$
FFT block size	1024 samples	Grid resolution	0.01 m
FFT window	Hanning, 50% overlap	Grid points	51 × 51

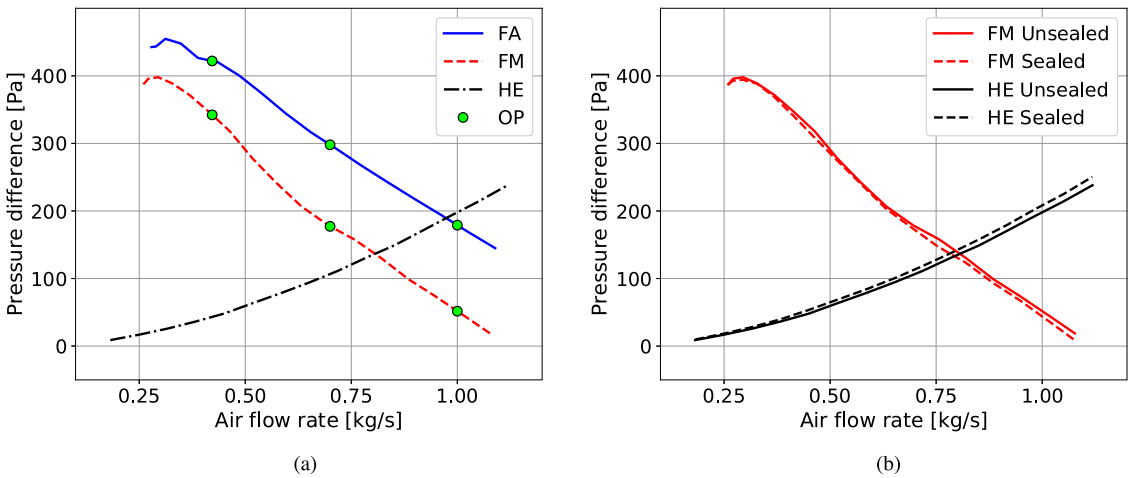

Fig. 5. Performance curves for the automotive cooling module. (a) Chosen unsealed OP for the FA and FM configurations. (b) Effect of sealing the open gap between the casing and the heat exchanger.

The first operating point is picked at $q_m = 0.42\,\text{kg s}^{-1}$, which is right after the stall region in order to avoid possible instabilities and the so-called stall noise appearance [5]. The second operating point is at $q_m = 0.7\,\text{kg s}^{-1}$, corresponding to the fan-alone maximum-efficiency point. The last, at $q_m = 1\,\text{kg s}^{-1}$, is close to the air extraction limit provided by the auxiliary fan. The curves depicted in Fig. 5(a) are measured with two static pressure sensors across the lab middle-wall partition. The fan is always run with a quasi-constant rotational speed of 3400 ± 50 rpm. An open gap of approximately 1 cm is present between the heat exchanger and the fan casing. Hence, part of the air sucked in by the fan might come from this area rather than pass through the heat exchanger. In order to study the influence of this open space over the performance curves, we sealed it and plotted in Fig. 5(b) the pressure difference against the mass flow rate for the radiator-and-casing (HE) configuration and for the FM configuration. Since no relevant discrepancies appear between the sealed and unsealed cases, the following study is focused on the unsealed setups, typically used in real applications.

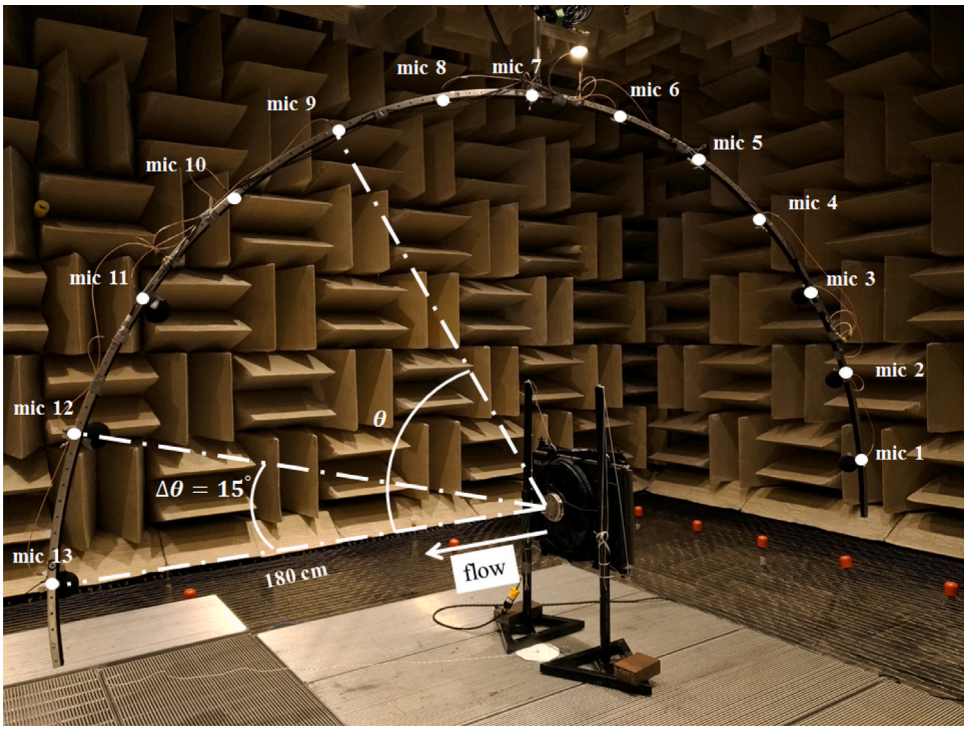

Fig. 6. Experimental setup for the directivity measurements at UdeS.

3.5. UdeS experimental campaigns

Acoustic directivity and source-localization measurements have been conducted on the same engine cooling module (FM) without sealing in the anechoic open-jet wind tunnel at Université de Sherbrooke (UdeS). More details about the wind tunnel can be found in [49]. The module measurements have been carried out in free-field conditions. All results obtained at UdeS are presented with a distance correction corresponding to 2.5 d_{fan}, i.e. the fan-microphone array distance at VKI.

3.5.1. Directivity setup and acquisition

The arc with a radius of 1.8 m is instrumented with 13 B&K 1/4" microphones (with a frequency range of 50 Hz to 10 kHz) and is hanged from the ceiling of the anechoic chamber as shown in Fig. 6. The microphones are distributed from 0° to 180° with a step of $\Delta\theta = 15°$ between two consecutive microphones. The hub of the rotor is located at the center of the arc. Microphones 1 and 13 are aligned perpendicularly to the fan plane. The arc is rotated clockwise with respect to its center with a step of 15°. At each step, the signals from all microphones are recorded for 30 s with a sampling frequency of 65.536 kHz. The wind-tunnel nozzle is covered with foam to minimize reflections and keep the excellent anechoic properties of the chamber. The arc itself has a layer of foam facing the central point. Windscreens are employed on the downstream microphones to minimize the influence of the flow. The directivity tests are conducted at the nominal rotational speed of 3400 rpm. Complementary measurements have been done at 1500 rpm, 2000 rpm, and 2400 rpm. The rotational speed measured with a tachometer is quasi-constant (variation of ±1.5% rpm). Far-field sound pressure levels (SPL) have been obtained with the Welch method (block size of 1048 samples with Hanning window and 50 % overlap).

3.5.2. Source-localization setup

An antenna with a diameter of 0.9 m instrumented with 60 B&K 1/4" microphones is used for the source-localization measurements at UdeS. The microphone array, shown in Fig. 7(a), is at the distance of 0.88 m and faces the heat exchanger. A tachometer is located downstream of the module to register the rotational speed of the fan. The signals are recorded for 30 s with a sampling frequency of 65.536 kHz. Tests have been run at 1500 rpm, 2000 rpm, 2400 rpm, and 3400 rpm. Only results at the nominal rotational speed are presented here.

Since the microphone array of UdeS is slightly smaller in diameter with respect to that installed at VKI (see the distribution of the electrets in Fig. 7(b)), the Rayleigh criterion calculated through Eq. (5) is expected to yield a higher source-separation frequency in this case, as will be discussed in Section 4.3.

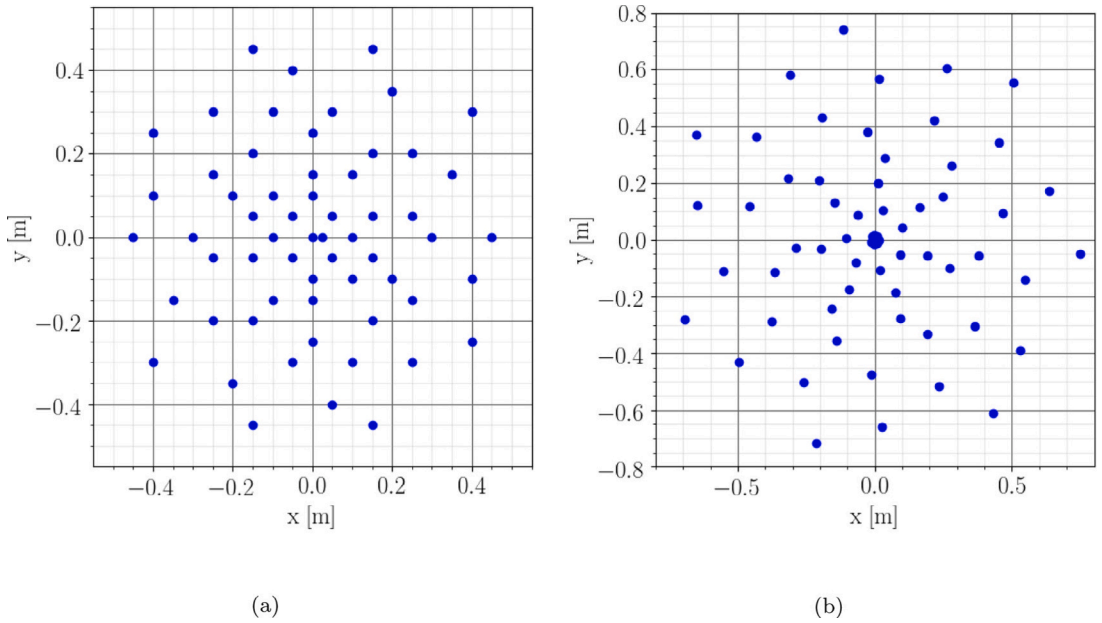

Fig. 7. (a) 60 microphones array for the source-localization measurements at UdeS. (b) 64 electret microphones are shown for the VKI antenna.

4. Results and discussion

The following section presents an overview of the acoustic properties of the FA and FM configurations by providing single-microphone measurements and sound-source localization maps. For the latter, a two-dimensional rectangular scanning grid is defined to fully encompass the rotational plane of the fan, with $x = \pm 0.25\,\mathrm{m}$, $y = \pm 0.25\,\mathrm{m}$. The resolution of the scanning grid is set to be $0.01\,\mathrm{m}$ in both directions. A dynamic range of $5\,\mathrm{dB}$ for all the following sound maps is adapted according to the maximum value in the specific map as the upper limit. Moreover, the displayed levels correspond to the sound pressure level at $1\,\mathrm{m}$ of distance from the low-speed cooling fan.

4.1. Single-microphone measurements

The far-field sound spectra, recorded at VKI by the microphone aligned with the center of the fan working at $q_m = 0.42\,\mathrm{kg\,s^{-1}}$, $0.7\,\mathrm{kg\,s^{-1}}$, and $1\,\mathrm{kg\,s^{-1}}$, are depicted in Figs. 8(a), 8(b), and 8(c), respectively. This location corresponds to a specification typically required by car manufacturers. For all flow-rate cases, the background noise (not reported in the graphs) is negligible compared to the fan sound radiation. Except for the case operating at $q_m = 1\,\mathrm{kg\,s^{-1}}$ above $4\,\mathrm{kHz}$, the fan alone always radiates more noise compared to the full module. Nevertheless, this difference is always less than $3\,\mathrm{dB}$ above $2\,\mathrm{kHz}$. Below this limit, some differences are found around the BPF and harmonics tonal peaks, which are broadened in the FA case. In fact, the sub-harmonics humps for these cases are more prominent. This can be attributed to the fact that the heat exchanger acts as a flow straightener, breaking down larger vortical structures upstream of the chamber and making the BPF much sharper [17,50]. Despite this effect, the presence of the heat exchanger does not seem to have a relevant impact on the shape of the spectra for the investigated conditions. This was also clearly observed by Rynell et al. [17] on a truck module with a similar heat-exchanger technology. Yet, an opposite trend has been recently reported by Czwielong et al. [51], who observed larger subharmonic humps and higher tonal peaks in the module case. The present evidence could be mostly explained by the different heat-exchanger technology used in this experiment, with larger and fewer tubes and less dense fin-and-louver arrangement. Consequently, the heater core no longer acts as an efficient turbulence control screen and may actually generate extra-large structures. These have time to develop till the fan inlet as the distance between the heat-exchanger core and the fan is also much larger.

In Fig. 8(d), the spectrum recorded at VKI for the FM case working at $q_m = 1\,\mathrm{kg\,s^{-1}}$ is compared with the spectrum recorded at UdeS for the FM case working at $3400\,\mathrm{rpm}$ in free-field conditions, namely at $\Delta P = 0\,\mathrm{Pa}$. These two operating points are close to each other, as can be noticed from the performance curve given in Fig. 5(a). The spectral shape is globally conserved with generally similar amplitudes, despite small variations at low frequencies mainly due to the different properties of the anechoic chambers, and the appearance of a dip at $7\,\mathrm{kHz}$ for the UdeS curve. The latter is an acoustic installation effect, proven to be independent of the axial fan rpm variation, as shown in the following section.

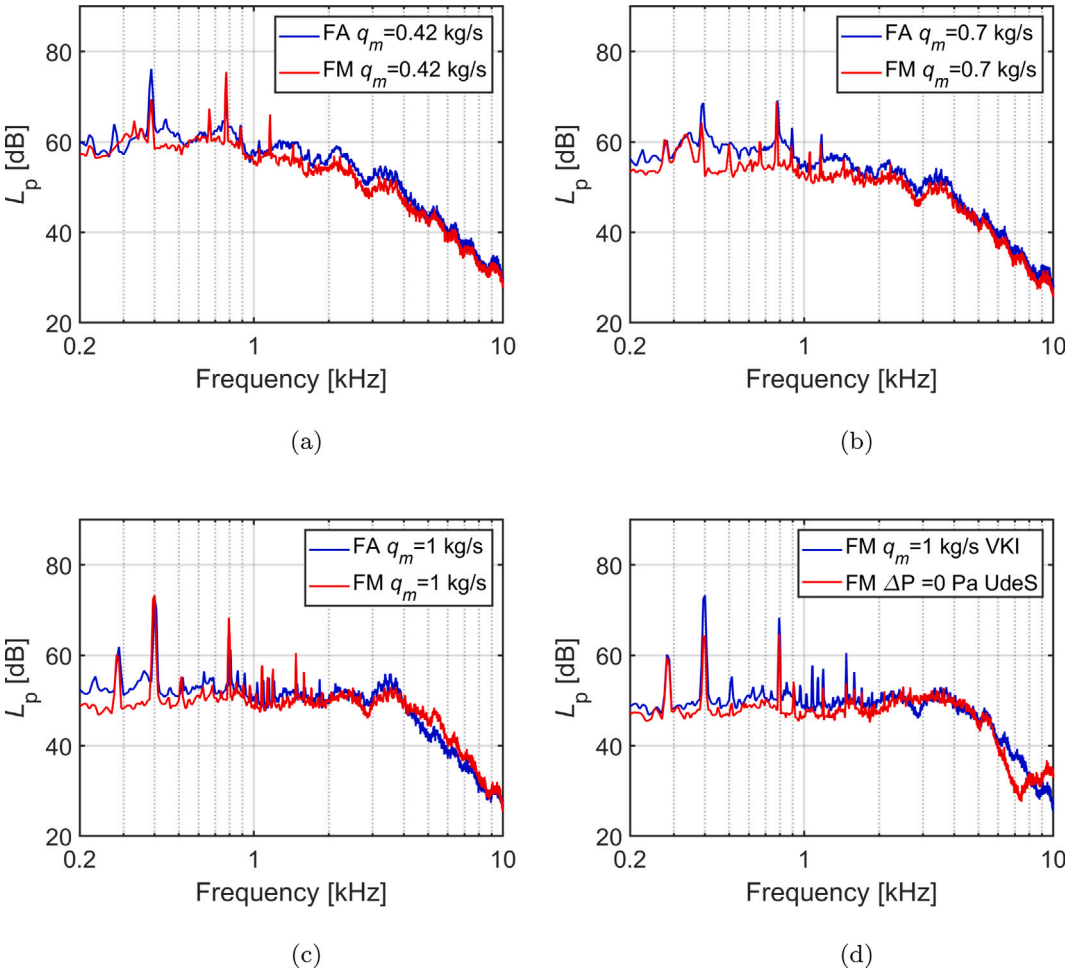

Fig. 8. Far-field acoustic spectra recorded at VKI by the microphone aligned with the center of the fan at a distance of $2.5d_{fan}$ of the FA and FM cases for the low (a), optimal (b), and high (c) airflow working points. The comparison between the FM VKI case at $1\,\mathrm{kg\,s^{-1}}$ and the UdeS FM case at 3400 rpm is shown in (d). The rotational speed for all the VKI cases is 3400 ± 50 rpm.

4.2. Directivity measurements

The spectra obtained at various rotational speeds during the directivity campaign are presented in Fig. 9(a). The shapes of the spectra are similar to each other for all the speeds, and we can notice three tones. For the case of 3400 rpm the tones corresponding to the first and second BPF are observed around 397 Hz and 793 Hz because of the above slight variation of rotational speed induced by the electrical motor (±50 rpm). An additional high tone is observed at 280 Hz, which is explained below. At high frequencies, beyond the roll-off at 4 kHz, the features of the spectra such as humps and peaks remain at the same frequencies and are independent of the variation of rotational speed. The acoustic wavelengths at these frequencies are comparable with the dimensions of the shroud and other components of the module. Therefore, we conclude that this part of the spectra is influenced by the experimental setup.

In Fig. 9(b), the SPL normalized by rpm^5 is shown versus the frequency normalized by BPF. The spectra collapse after the 2nd BPF (2*BPF in the figure), suggesting a dipole noise source. At lower frequencies (corresponding to a Strouhal number based on the tip chord length, St_t, up to 0.6), several tones corresponding to frequencies harmonics of the rotational frequency (5/rev, 9/rev, 12/rev, etc.) are observed. These harmonics can be attributed to the vibration of the module caused by a slight unbalance of the fan. Additional scaling with St_t is depicted in Fig. 9(c) for the SPL normalized by rpm^5. A good collapse is observed at Strouhal number around 1 (from 0.6 to 2) and points out that the noise source at the blade tip is chordwise compact at these frequencies. The power 5 is close to the exponent found by Canepa et al. [52] for the broadband and tip-leakage noise generated by such automotive engine cooling low-speed fans. Fig. 9(d) shows that the normalization with rpm^4 collapses the spectra at Strouhal from 2 to 4 at all the rotational speeds, except for the lowest speed. This highlights that the noise source becomes chordwise non-compact at high frequencies. The deviation of the case at 1500 rpm may be caused by some significant contribution of the motor. Surprisingly, a good collapse is also found at low Strouhal numbers up to 0.5, even though it corresponds to the frequency range strongly influenced by vibrations.

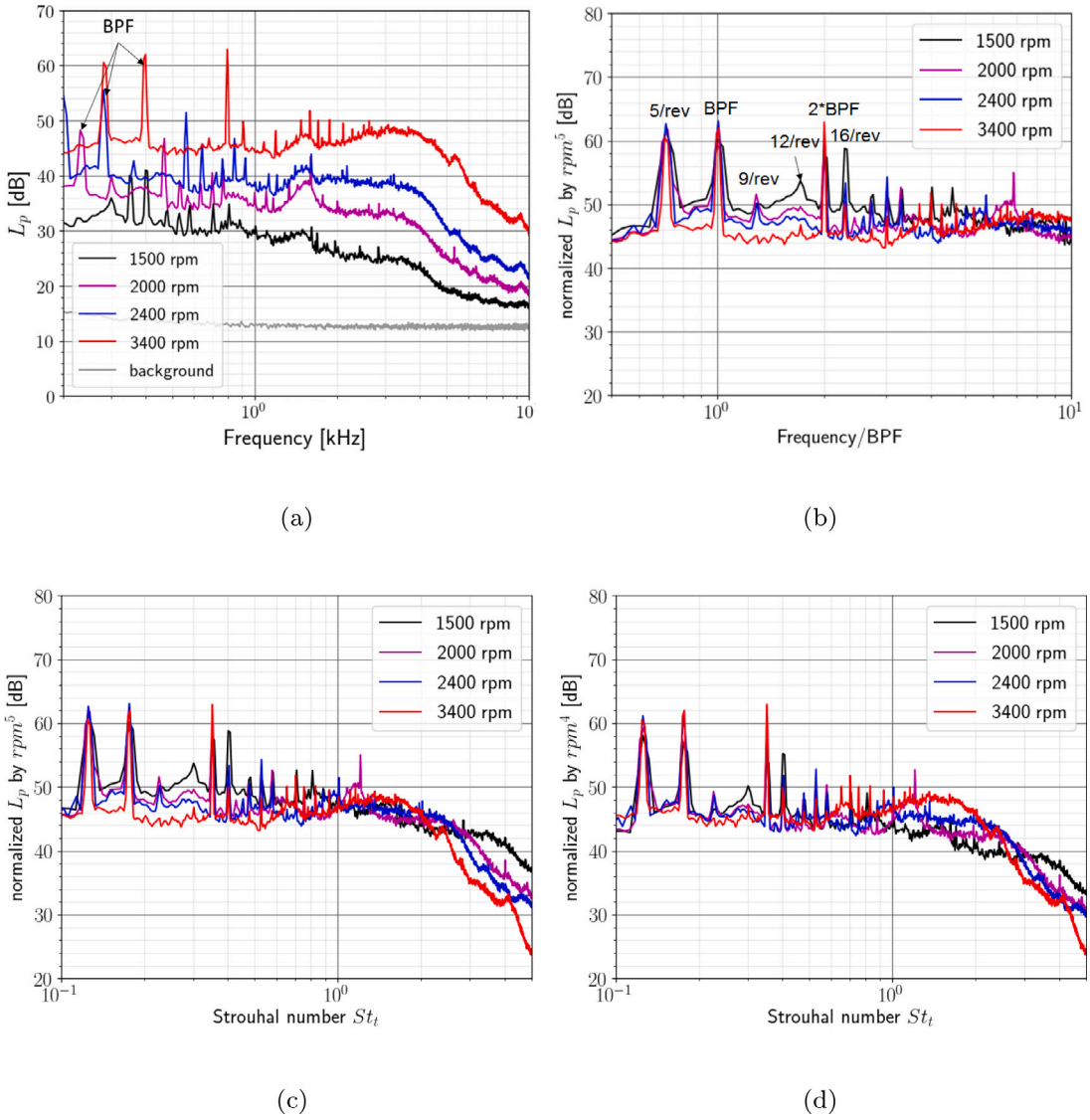

Fig. 9. Directivity results obtained at UdeS. (a) SPL of the antenna most-centered microphone at various rotational speeds. (b) Normalized SPL by rpm^5 versus frequency normalized by BPF. Normalized SPL by (c) rpm^5 and (d) rpm^4 versus the Strouhal number based on the tip chord.

In Fig. 10, the radiation map (frequency versus observation angles) is shown for the arc at 0° with the flow direction from 0° (microphone 1) to 180° (microphone 13). The BPF is observed for all angles and has a higher level in the upstream direction. The harmonic tone at lower frequencies is more pronounced at angles close to the fan axis. It is worth noting that the peak of the 2nd BPF has much higher levels upstream than downstream. At high frequencies beyond 4 kHz, the roll-off appears. Overall, the map is symmetric with respect to 90° and presents two lobes of sound radiation, which is another evidence of the dipole source.

4.3. Sound-source localization maps and integrated spectra

In this section, the sound-source localization maps carried out at VKI for the FM at $q_m = 1\,\mathrm{kg\,s^{-1}}$ are compared with those calculated at UdeS for the FM at $\Delta P = 0\,\mathrm{Pa}$. These operating points are close to each other, and so it is possible to evaluate the repeatability of the ROSI method implementation by localizing and quantifying the noise sources. In Fig. 11, the sound maps are depicted for third-octave bands with center frequencies of 2.5 kHz, 3.15 kHz, and 4 kHz.

For frequencies above 3.15 kHz in the VKI case, the maximum L_p appears to be toward the tip of the blade. As frequency increases, a better spatial resolution of the map can be obtained, and more details can be observed. In contrast, at 2.5 kHz and below, the identification of the aerodynamic sources for each blade separately is not achievable, and the sound sources cannot be attributed to a specific noise mechanism. This shows the limitation of the measurement technique in resolving sound sources at low frequencies.

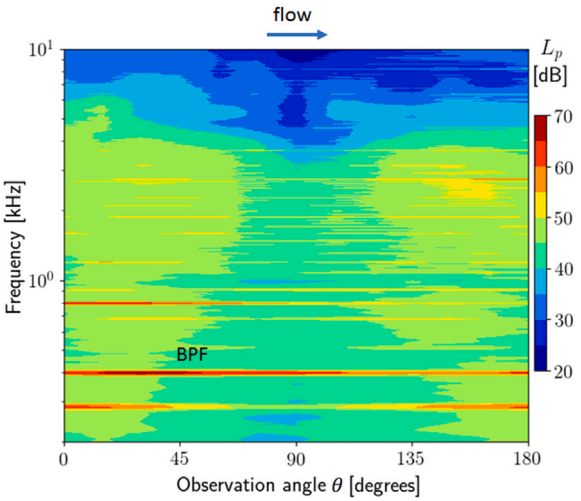

Fig. 10. Frequency versus observation angle θ map at 3400 rpm.

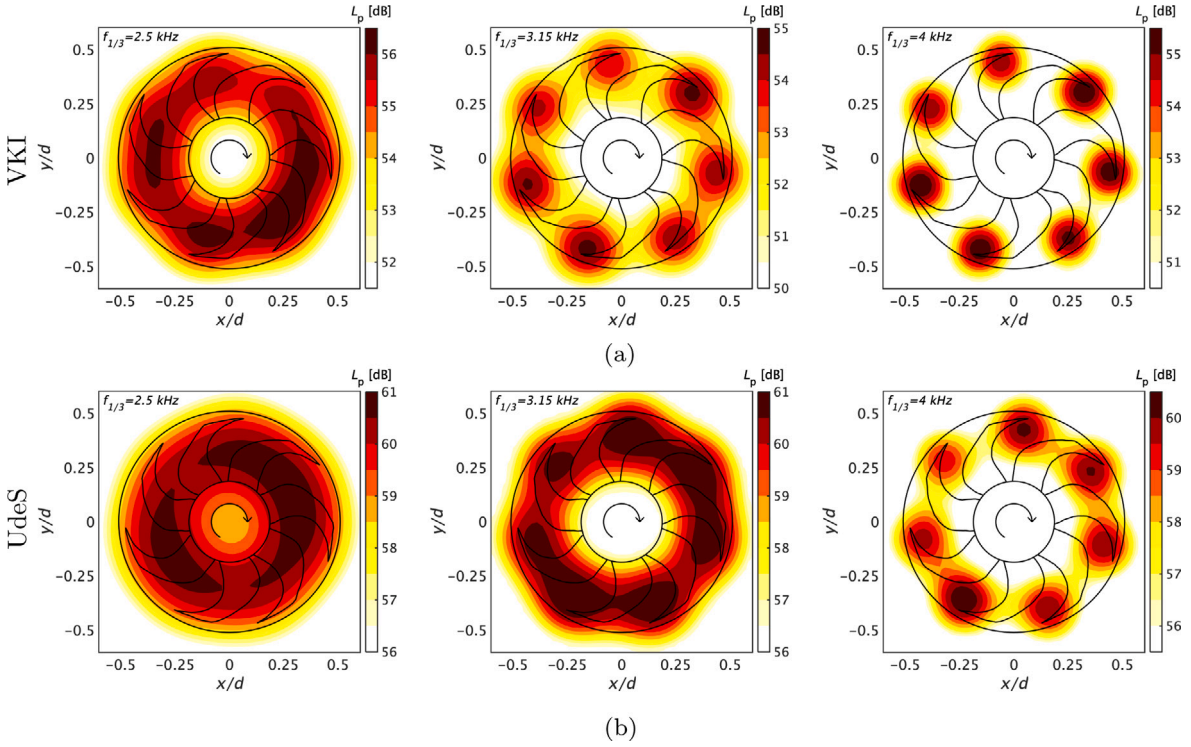

Fig. 11. Comparison between sound-localization maps at different frequency bands: (a) sound maps computed at VKI for the FM at $q_m = 1\,\mathrm{kg\,s^{-1}}$, and (b) sound maps calculated at UdeS for the FM at $\Delta P = 0\,\mathrm{Pa}$.

The present evidence can be further examined by using the Rayleigh criterion explained in Section 3.3. If the distance between two consecutive blades $R = 0.10\,\mathrm{m}$ is considered as the minimum separation distance of two sources, through Eq. (5) the resulting frequency is $f_{min} \approx 2.50\,\mathrm{kHz}$ for the VKI antenna. This result is verified by the VKI beamforming maps in Fig. 11: at 2.5 kHz as centered frequency, the sound source map is affected by the frequencies which are lower than the f_{min} and the contribution of each blade is not identified clearly. Nevertheless, at 3.15 kHz, where all the frequencies of the band are above the Rayleigh criterion, the noise-source locations can be detected for each blade. Similar considerations can be made for the UdeS sound maps: in this case, Eq. (5) yields a higher frequency of $f_{min} \approx 3.66\,\mathrm{kHz}$ considering the same $R = 0.10\,\mathrm{m}$. As a consequence, clean acoustic source separation is visible only for $f \geq 3.15\,\mathrm{kHz}$. Although for the maps centered at 2.5 kHz it is hard to infer the azimuthal location

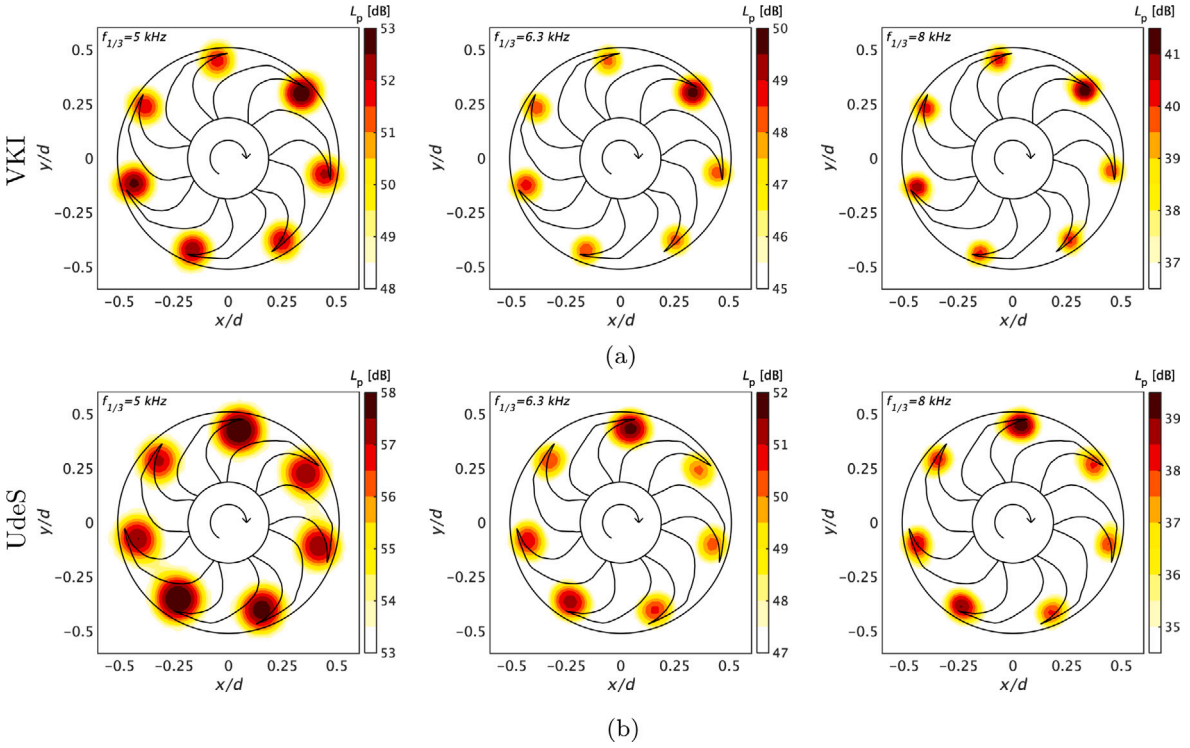

Fig. 12. Comparison between sound-localization maps at different frequency bands: (a) sound maps computed at VKI for the FM at $q_m = 1\,\mathrm{kg\,s^{-1}}$, and (b) sound maps calculated at UdeS for the FM at $\Delta P = 0\,\mathrm{Pa}$.

of the sources, we remark that these appear mostly at the mid-span region of the blade. The sound maps at this frequency band for other operating points are not shown here for the sake of conciseness, but this trend is always observed with and without the heat exchanger. For the studied axial fan, the importance of this blade region in terms of sound emissions was highlighted in [53], especially for frequencies below 3 kHz, where a dominance of the leading-edge noise mechanism was attributed to the high turbulent-kinetic-energy development in such a loaded blade area.

In Fig. 12, the comparison between the VKI and UdeS cases is carried out at higher third-octave frequency bands, namely at 5 kHz, 6.3 kHz, and 8 kHz. For all the cases, the noise sources are clearly located at the tip of the blades and, in particular, at the leading edge.

If we can infer the similarity of the source locations for the VKI and UdeS cases by comparing the sound maps, the integrated spectra in Fig. 13(a) show quantitatively the amplitude levels with respect to the microphone aligned with the center of the fan. The results are obtained through a summation of the mapped sound pressure levels over the regions where sources with 1.5 dB dynamic range are included. The dynamic range value can be justified by the fact that spurious sources have to be subtracted in the summation, or else a wrong reconstructed L_p would be calculated. Moreover, the summation refers to the squared pressure values since all potential sources placed in the SG are assumed to be statistically incoherent, as typically done in conventional beamforming algorithms [47].

As expected, for both VKI and UdeS cases, an erroneous source reconstructed level is found at low frequency. This is due to the poor spatial resolution of the source region that does not allow for proper separation of the different noise contributions coming from the blades, as mentioned in Section 3.3. Indeed, the presence of overlapping contributions in the integration region leads to an overestimation of the actual sound level that is inversely proportional to the frequency: the lower the frequency, the poorer the spatial resolution and the higher the overestimation. However, for higher frequencies, the algorithm is able to separate the noise contributions correctly, and the single-microphone and the ROSI curves exhibit a fairly good agreement for both VKI and UdeS cases. This trend can be further verified from Fig. 13(b), where the relative differences on the L_p are depicted for the range between 3.15 kHz and 8 kHz. The VKI maps exhibit a satisfactory agreement above 4 kHz, with the smallest difference of about 1 dB at 6.3 kHz. Although UdeS maps exhibit more than 5 dB of divergence at 6.3 kHz due to the Rayleigh criterion, the same trend of VKI maps is followed, showing the best agreement (less than 1 dB of difference) at 8 kHz.

4.4. Sound-source localization maps varying the operating conditions

In Fig. 14, we illustrate the source distribution maps of the reconstructed SPL for the FA and FM configurations at three different volumetric flow rates. These maps are obtained at VKI, and, for the sake of conciseness, only those at 6.3 kHz are shown considering that this is the third-octave frequency band with the best visualization of the results, as highlighted in the previous paragraph.

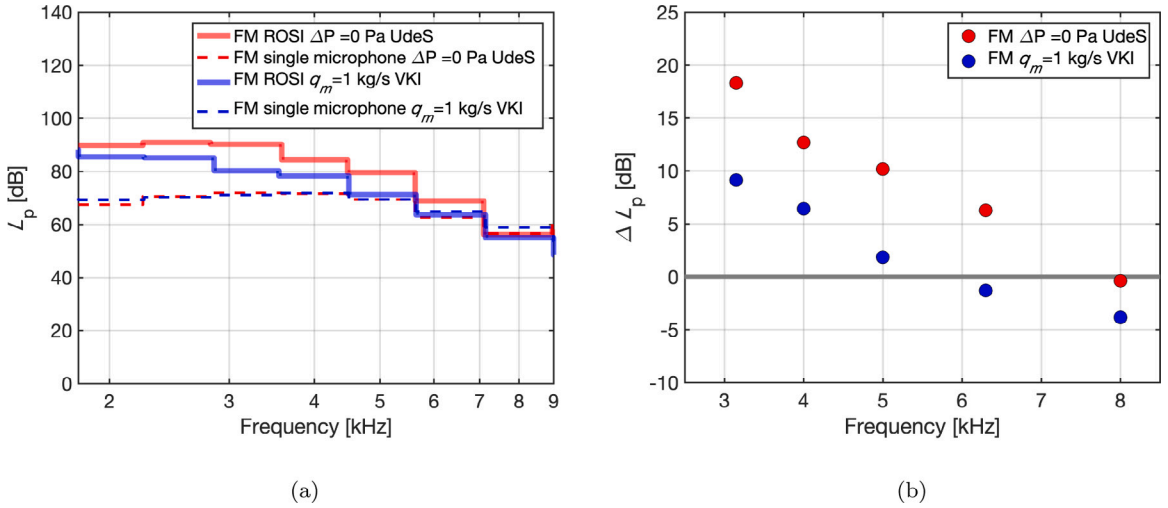

Fig. 13. Comparisons between the VKI FM-case operating at $q_m = 1\,\mathrm{kg\,s^{-1}}$ and the FM UdeS-case working at $\Delta P = 0\,\mathrm{Pa}$. (a) Integrated spectra (solid lines) and the single-microphone spectra (dashed lines); (b) relative differences of the reconstructed L_p by ROSI and that recorded by the microphone aligned with the center of the fan.

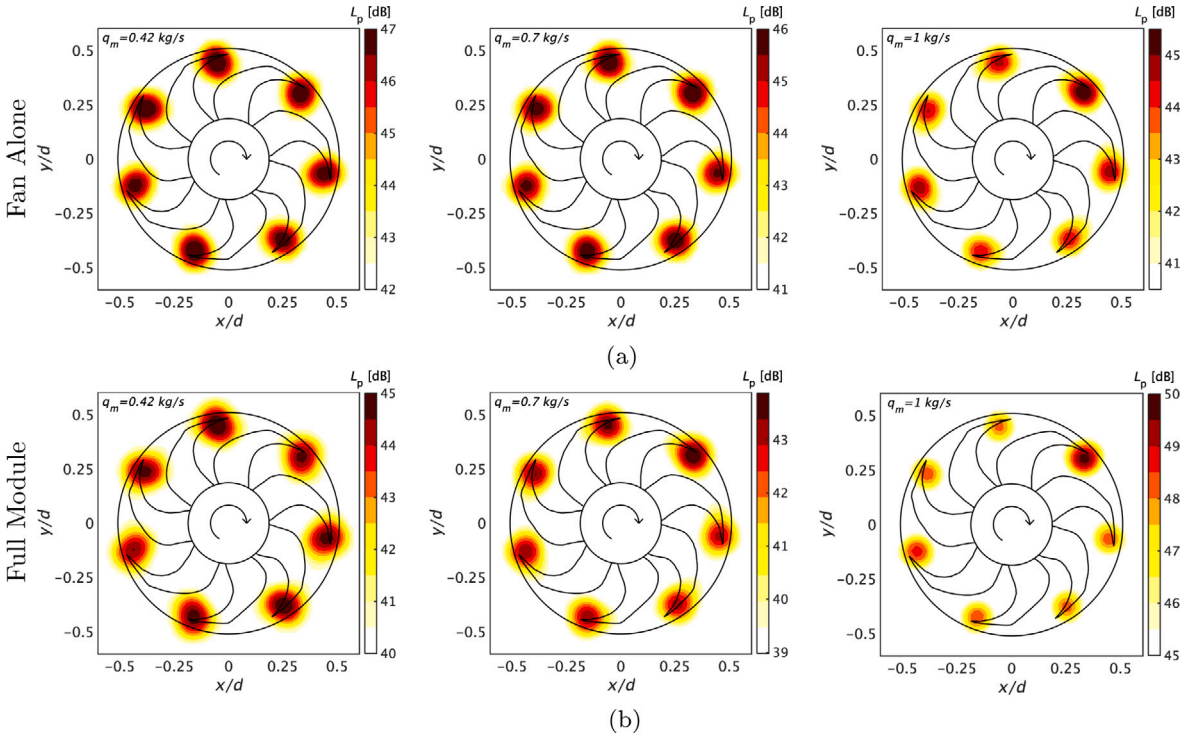

Fig. 14. Sound-localization maps carried out at VKI at 6.3 kHz varying the operating condition in a FA (a) or FM configuration (b).

The presence of the radiator for the three FM operating points allows for the reconstruction of the acoustic sources, suggesting that the masking effect of this component can be neglected. To the authors' knowledge, this work is the first attempt to reconstruct the rotating sound sources through a radiator. Finally, the integrated spectra for FA and FM operating under different conditions are shown in Fig. 15 along with the relative differences of L_p. For all the working conditions, the comparison of the integrated spectra against the single-microphone measurement aligned with the center of the fan is below 5 dB starting from the 5 kHz one-third frequency band.

As mentioned in Section 1, there are a handful of studies in the literature that use sound-source maps to identify the dominant sound generation mechanism in a specific frequency range. Fans with different geometries often lead to a different distribution

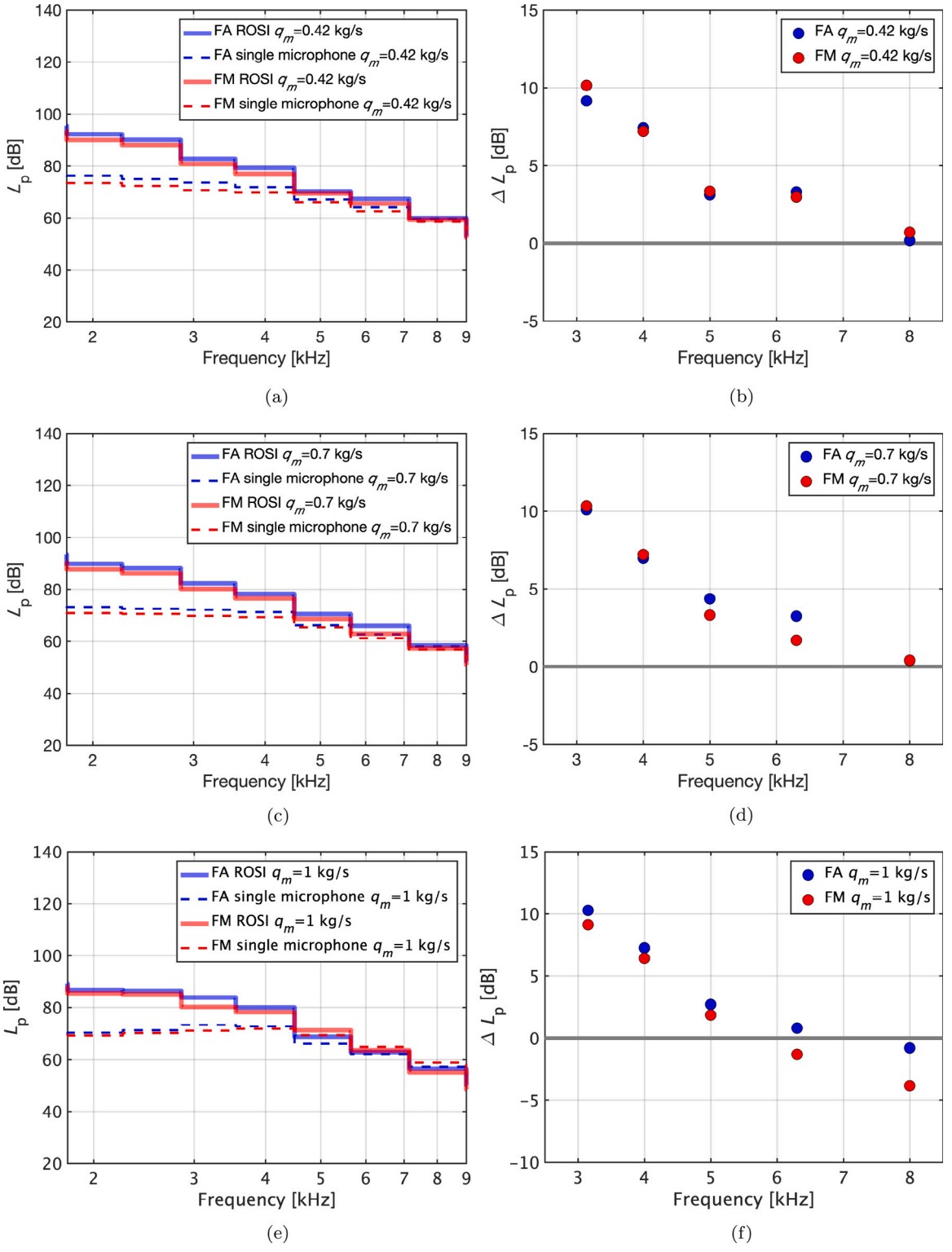

Fig. 15. The FA and FM integrated spectra (solid lines) and the single-microphone spectra (dashed lines) are compared at varying operating conditions. The circles represent the relative differences of the reconstructed L_p by ROSI and that recorded by the microphone aligned with the center of the fan.

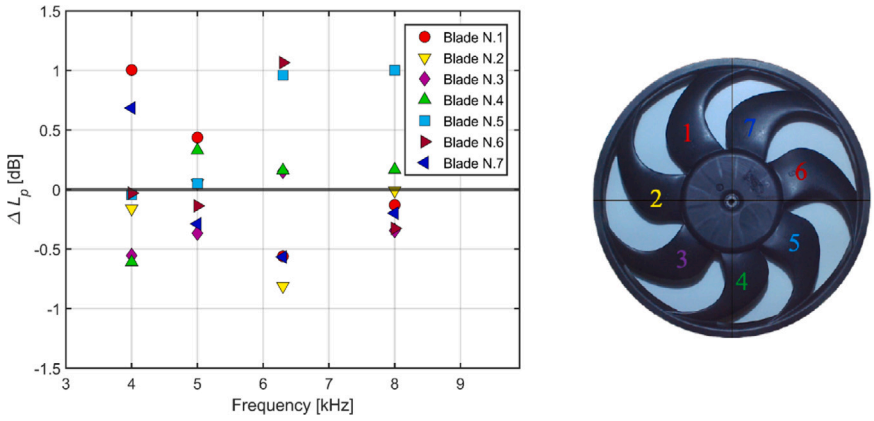

Fig. 16. Relative differences in sound pressure level for each blade with respect to the reference value $L_{p,ref(1/3)}$ and the numbered blades of the fan.

of sources in the plane of rotation. In particular, the effect of the blade forward or backward curvature is a major contributor to this difference [28,36]. Although it is not trivial to make comparisons between fans with different geometry, Zenger et al. [18] demonstrated with a rotating beamforming technique that, for a forward-skewed axial fan, sources distribute (at high frequencies) mainly at the tip of the blade leading edges only in the case where the inlet inflow conditions are strongly distorted. In contrast, with clean inlet inflow conditions, sources still tend to distribute at the tip of the blade, where higher relative velocities are reached, but at the trailing edge. This evidence, in agreement with classical studies involving axial fan noise [5,6], indicates turbulence-interaction noise as the dominant one under distorted inflow conditions, whereas the self-noise is dominant under clean inflow conditions.

In the present case, above 2.5 kHz, the sources are distributed clearly at the tip of the blade at the leading edge for each tested operating condition, which is also consistent with the study performed on a forward-swept engine cooling fan by Sanjose and Moreau [54]. Hence, turbulence-interaction noise appears to be the dominant noise-source contribution in this type of axial fan, at least in the frequency range investigated by the ROSI technique. Nevertheless, as already hinted at by the similarity between the frequency spectra in Fig. 8, the presence of the radiator has no visible effect on the position of the sound sources. This suggests that the turbulence produced downstream of the radiator is either not characterized by high intensity or is dissipated before interacting with the blades. As a consequence, most of the turbulence is likely produced within the gap between the shroud and the fan rather than directly coming from the radiator. As Herold et al. [55] found, we can expect a displacement of the sources toward the leading edge of the blade for moderate air flows. For these operating points, the blades are sufficiently loaded such that the recirculation flow at the tip becomes significant. In fact, as pointed out in [3], these plastic-made ventilators can be subjected to substantial deformation during the rotation that can result in a flow in the blade tip regions amounting to 6 % of the total mass flow through the fan. This phenomenon is expected to occur also in the present case, regardless of the L-shaped ring geometry, which is designed to reduce the recirculation flow in this area of the blade [12]. Thus, we infer that this secondary flow is crucial to the generation of the noise not only at low-to-mid frequencies as commonly accepted in the literature but also at high frequencies, as the sound-source maps demonstrate.

4.5. Acoustic contribution of each blade

The validation of the previous quantitative results gives the possibility to rely on the quantitative estimation of specific parts of the sound-source maps. For this reason, an analysis of the acoustic contribution of each blade is considered in the range of 4 kHz to 8 kHz with the same strategy adopted for the calculation of the integrated spectrum (Fig. 15). For each blade, an integration region with a dynamic range of 1.5 dB is taken into account. All computed integrated spectra have been compared with a reference one. The latter is calculated by dividing the total integrated spectra retrieved in the previous section by the total number of blades ($B = 7$). The division is performed considering the squared pressure values.

The relative differences of the integrated spectra between the blades and the reference are illustrated in Fig. 16. Since it is not possible to observe a significant difference in noise emission among the blades (less than ± 1 dB for the examined frequencies), it can be concluded that each blade contributes to the overall radiated noise in a similar way. This is not a foregone conclusion since the fan blades are not perfectly equally spaced. Furthermore, it would not be possible to infer such a conclusion with standard microphone measurements.

5. Conclusions

In the automotive industry, the engine cooling module is a major contributor to overall automotive noise emissions. To fully characterize the latter in a well-controlled environment, sound-pressure measurements have been performed on the same module in two different anechoic wind tunnels using arrays of microphones, building a unique experimental database on such systems.

At UdeS, the module has been tested in free-flow conditions providing directivity data at various rotational speeds. At VKI, measurements on the fan-alone (FA) and on the full module (FM) have further provided narrow-band spectra at different operating conditions. The former case has allowed for some scaling analysis, which has clearly stressed the dipolar nature of the sound emitted by the module and confirmed previous broadband and tip-noise results [52]. The latter case has shown the evolution of the SPL with flow rate: the more loaded the fan is, the more broadband the spectrum is, with a more significant contribution at lower frequencies. This is similar to what is observed in airfoil noise with increasing incidence [56,57] and confirms previously reported sound power measurements in reverberant wind tunnels [12,58].

The comparison between the FA and the FM cases shows that the overall bell shape of the broadband component is similar for the same inflow condition, except at lower frequencies around the BPF tones. Indeed, the trend on the tones with the increasing flow rate is similar, but their amplitudes and shapes differ. Some line broadening occurs on the fan alone, which is reduced on the module, the heat exchanger acting as a flow straightener or turbulence control screen. For the same free-flow conditions, both facilities yield comparable narrow-band spectra.

Additionally, source localization has been performed on the same module at the nominal speed and free-flow condition in both test facilities. Similar spiral microphone arrays have been used, the VKI one being slightly larger, yielding a better resolution at lower frequencies. This joint source localization study has also allowed investigating the influence that the suction-side radiator has on the distribution of sound sources and the transmission of acoustic waves passing through it. A time-based rotating beamforming technique, ROSI, has been implemented and used to localize and quantify the sound sources generated by the low-speed axial cooling fan.

In both test facilities, the sound sources are localized at the same position on the module at the tip blade leading edge, making it possible to distinguish the contribution of each blade from the 3.15 kHz one-third frequency band for the VKI case and 4 kHz for the UdeS one. This demonstrates the repeatability and robustness of the implemented noise-localization technique. Moreover, the presence of the radiator between the antenna and the fan does not prevent the correct reconstruction of the sound sources obtained with the ROSI technique. To the authors' knowledge, no previous attempt to perform rotating beamforming measurements through a radiator has been previously reported in the literature.

At VKI, the method has also been applied to the three operating points in both FM and FA cases, isolating the sources on the blades from the 3.15 kHz one-third frequency band. In all cases, the sound sources are always located at the leading edge of the blade tip. Therefore, for this particular engine cooling module, the turbulence-interaction noise generated by the secondary flow in the tip region appears to be the broadband noise mechanism that dominates the noise spectra at all the frequencies resolved by ROSI for all the studied flow rates. This confirms previously reported sound power predictions as a function of flow rates on a similar forward-swept ring fan that had been tested in a reverberant wind tunnel [12]. Note also that, in the present study, tip noise has primary importance not only at low-to-mid frequencies as generally pointed out in the literature [6] but also at high frequencies.

Finally, regardless of the different operating conditions, the radiator appears to have a negligible influence on sound generation and propagation. Therefore, it can be seen as acoustically transparent with negligible transmission losses, as previously shown in LBM simulations.

CRediT authorship contribution statement

O. Amoiridis: Methodology, Software, Validation, Formal analysis, Investigation, Data curation, Writing – original draft, Writing – review & editing, Visualization. **A. Zarri:** Conceptualization, Methodology, Software, Validation, Formal analysis, Investigation, Data curation, Writing – original draft, Writing – review & editing, Visualization. **R. Zamponi:** Methodology, Software, Validation, Formal analysis, Data curation, Writing – original draft, Writing – review & editing. **Y. Pasco:** Software, Validation, Formal analysis, Data curation. **G. Yakhina:** Methodology, Software, Formal analysis, Data curation, Writing – original draft, Writing – review & editing, Visualization. **J. Christophe:** Conceptualization, Resources, Supervision, Project administration, Funding acquisition. **S. Moreau:** Conceptualization, Investigation, Writing – review & editing, Supervision. **C. Schram:** Conceptualization, Resources, Supervision, Project administration, Funding acquisition.

Declaration of competing interest

The authors declare that they have no known competing financial interests or personal relationships that could have appeared to influence the work reported in this paper.

Acknowledgments

The authors acknowledge the support of the European Commission's Framework Program "Horizon 2020", through the Marie Skłodowska-Curie Innovative Training Networks (ITN) "SmartAnswer - Smart mitigation of flow-induced acoustic radiation and transmission" grant agreement No. 722401 to the present research project. Furthermore, the authors acknowledge Valeo in France, for the received technical support on axial fans, as well as the Budapest University of Technology and Economics in Hungary, for the support concerning the implementation of the ROSI algorithm.

References

[1] J. Christophe, K. Kucukcoskun, C. Schram, Tonal and Broadband sound prediction of a locomotive cooling unit, in: 19th AIAA/CEAS Aeroacoustics Conference, American Institute of Aeronautics and Astronautics, Berlin, Germany, 2013, http://dx.doi.org/10.2514/6.2013-2180.
[2] S. Allam, M. Åbom, Noise reduction for automotive radiator cooling fans, Configurations 15 (2015) 17.
[3] M. Henner, B. Demory, M. Alaoui, M. Laurent, B. Behey, Effect of blade curvature on fan integration in engine cooling module, Acoustics 2 (4) (2020) 776–790, http://dx.doi.org/10.3390/acoustics2040043.
[4] S. Caro, S. Moreau, Aeroacoustic modelling of low pressure axial flow fans, in: 6th Aeroacoustics Conference and Exhibit, 2000, p. 2094.
[5] A. Guédel, Acoustique des Ventilateurs, PYC Livres, Villeurbanne, France, 1999.
[6] S. Moreau, M. Roger, Competing broadband noise mechanisms in low-speed axial fans, AIAA J. 45 (1) (2007) 48–57.
[7] S. Magne, S. Moreau, A. Berry, Subharmonic tonal noise from backflow vortices radiated by a low-speed ring fan in uniform inlet flow, J. Acoust. Soc. Am. 137 (1) (2015) 228–237.
[8] T. Carolus, M. Schneider, H. Reese, Axial flow fan broad-band noise and prediction, J. Sound Vib. 300 (1–2) (2007) 50–70.
[9] I.J. Sharland, Sources of noise in axial flow fans, J. Sound Vib. 1 (3) (1964) 302–322.
[10] M. Roger, S. Moreau, Broadband self noise from loaded fan blades, AIAA J. 42 (3) (2004) 536–544.
[11] T. Carolus, Ventilatoren-aerodynamischer entwurf, schallvorhersage, Konstruktion 2 (2003).
[12] S. Moreau, M. Sanjose, Sub-harmonic broadband humps and tip noise in low-speed ring fans, J. Acoust. Soc. Am. 139 (1) (2016) 118–127.
[13] E. Canepa, A. Cattanei, F.M. Zecchin, G. Milanese, D. Parodi, An experimental investigation on the tip leakage noise in axial-flow fans with rotating shroud, J. Sound Vib. 375 (2016) 115–131.
[14] M. Piellard, B. Coutty, V. Le Goff, F. Pérot, V. Vidal, Direct aeroacoustics simulation of automotive cooling fan system: Effect of upstream geometry on broadband noise, in: 20th AIAA/CEAS Aeroacoustics Conference, AIAA 2014-2455 paper, Atlanta, GA, 2014.
[15] D. Lallier-Daniels, M. Sanjosé, S. Moreau, M. Piellard, Aeroacoustic study of an axial engine cooling module using lattice-Boltzmann simulations and the Ffowcs Williams and Hawkings' analogy, Eur. J. Mech. B 61 (2017) 244–254.
[16] S. Allam, M. Åbom, Acoustic modelling and characterization of plate heat exchangers, 2012, http://dx.doi.org/10.4271/2012-01-1562.
[17] A. Rynell, G. Efraimsson, M. Chevalier, M. Abom, Acoustic characteristics of a heavy duty vehicle cooling module, Appl. Acoust. 111 (2016) 67–76, http://dx.doi.org/10.1016/j.apacoust.2016.04.004.
[18] F. Zenger, G. Herold, S. Becker, Acoustic characterization of forward-and backward-skewed axial fans under increased inflow turbulence, AIAA J. 55 (4) (2017) 1241–1250.
[19] F.J. Zenger, A. Renz, M. Becher, S. Becker, Experimental investigation of the noise emission of axial fans under distorted inflow conditions, J. Sound Vib. 383 (2016) 124–145, http://dx.doi.org/10.1016/j.jsv.2016.07.035.
[20] B. Coutty, S. Moreau, Aeroacoustic modeling of an automotive engine cooling module, in: 26th International Congress on Noise and Vibration, Montreal, Canada, paper 525, 2019, Montreal, Canada.
[21] D. Lallier-Daniels, Analysis of Tip Leakage Flow Noise Inception in Axial Fans (Ph.D. thesis), Université de Sherbrooke, Sherbrooke, Canada, 2018.
[22] P. Sijtsma, S. Oerlemans, H. Holthusen, Location of rotating sources by phased array measurements, in: 7th AIAA/CEAS Aeroacoustics Conference and Exhibit, 2001, p. 2167.
[23] S. Oerlemans, P. Sijtsma, B.M. López, Location and quantification of noise sources on a wind turbine, J. Sound Vib. 299 (4–5) (2007) 869–883.
[24] P. Sijtsma, Using phased array beamforming to identify broadband noise sources in a turbofan engine, Int. J. Aeroacoust. 9 (3) (2010) 357–374.
[25] W. Pannert, C. Maier, Rotating beamforming–motion-compensation in the frequency domain and application of high-resolution beamforming algorithms, J. Sound Vib. 333 (7) (2014) 1899–1912.
[26] G. Herold, E. Sarradj, Microphone array method for the characterization of rotating sound sources in axial fans, Noise Control Eng. J. 63 (6) (2015) 546–551.
[27] R. Dougherty, B. Walker, Virtual rotating microphone imaging of broadband fan noise, in: 15th AIAA/CEAS Aeroacoustics Conference (30th AIAA Aeroacoustics Conference), 2009, p. 3121.
[28] F.J. Zenger, G. Herold, S. Becker, E. Sarradj, Sound source localization on an axial fan at different operating points, Exp. Fluids 57 (8) (2016) 136.
[29] S. Jekosch, E. Sarradj, An extension of the virtual rotating array method using arbitrary microphone configurations for the localization of rotating sound sources, in: Acoustics, Vol. 2, Multidisciplinary Digital Publishing Institute, 2020, pp. 330–342.
[30] G. Kotán, B. Tóth, J. Vad, Comparison of the rotating source identifier and the virtual rotating array method, Period. Polytech.-Mech. Eng. 62 (4) (2018) 261–268.
[31] O. Minck, N. Binder, O. Cherrier, L. Lamotte, V. Pommier-Budinger, Fan noise analysis using a microphone array, in: Fan 2012 - International Conference on Fan Noise, Technology and Numerical Methods, April, 2012, pp. 1–9.
[32] T. Benedek, P. Tóth, Beamforming measurements of an axial fan in an industrial environment, Period. Polytech.-Mech. Eng. 57 (2) (2013) 36–46.
[33] T. Benedek, J. Vad, An industrial onsite methodology for combined acoustic-aerodynamic diagnostics of axial fans, involving the phased array microphone technique, Int. J. Aeroacoust. (2016).
[34] B. Tóth, J. Vad, Algorithmic localisation of noise sources in the tip region of a low-speed axial flow fan, J. Sound Vib. 393 (2017) 425–441.
[35] G. Herold, E. Sarradj, Frequency domain deconvolution for rotating sources on an axial fan, in: 6th Berlin Beamforming Conference, February, 2016, pp. 1–8.
[36] G. Herold, F. Zenger, E. Sarradj, Influence of blade skew on axial fan component noise, Int. J. Aeroacoust. 16 (4–5) (2017) 418–430.
[37] O. Amoiridis, R. Zamponi, A. Zarri, J. Christophe, C. Schram, Localization and characterization of rotating noise sources on axial fans by means of an irregularly shaped microphone array, J. Phys. Conf. Ser. 1909 (1) (2021) 012003, http://dx.doi.org/10.1088/1742-6596/1909/1/012003.
[38] G. Howell, A. Bradley, M. McCormick, J. Brown, De-dopplerization and acoustic imaging of aircraft flyover noise measurements, J. Sound Vib. 105 (1) (1986) 151–167.
[39] B. Barsikow, W. King, On removing the Doppler frequency shift from array measurements of railway noise, J. Sound Vib. 120 (1988) 190–196.
[40] A. Zarri, J. Christophe, C.F. Schram, Low-order aeroacoustic prediction of low-speed axial fan noise, in: 25th AIAA/CEAS Aeroacoustics Conference, 2019, p. 2760.
[41] Y. Lian, W. Shyy, Laminar-turbulent transition of a low Reynolds number rigid or flexible airfoil, AIAA J. 45 (7) (2007) 1501–1513.
[42] M. Bilka, J. Anthoine, C. Schram, Design and evaluation of an aeroacoustic wind tunnel for measurement of axial flow fans, JASA 130 (6) (2011) 3788–3796.
[43] J. Dominique, J. Christophe, C. Schram, An experimental multi-ports methodology for fan installation effects investigation, in: 24th AIAA/CEAS Aeroacoustics Conference, 2018, p. 3926.
[44] I. Standard, ISO 5167:2003, "Measurement of Fluid Flow by Means of Pressure Differential Devices Inserted in Circular Cross-Section Conduits Running Full - Parts 1,2,", International Organization for Standardization, 2003.
[45] R.P. Dougherty, Spiral-shaped array for broadband imaging, 1998, U.S. 5 838 284.
[46] L. Rayleigh, XXXI. Investigations in optics, with special reference to the spectroscope, Lond. Edinb. Dublin Philos. Mag. J. Sci. 8 (49) (1879) 261–274.
[47] T.J. Mueller, Aeroacoustic Measurements, Springer Berlin, 2002.

[48] R. Zamponi, S. Satcunanathan, S. Moreau, D. Ragni, M. Meinke, W. Schröder, C. Schram, On the role of turbulence distortion on leading-edge noise reduction by means of porosity, J. Sound Vib. 485 (2020) 115561, http://dx.doi.org/10.1016/j.jsv.2020.115561.
[49] T. Padois, P. Laffay, A. Idier, S. Moreau, Detailed experimental investigation of the aeroacoustic field around a Controlled-Diffusion airfoil, in: 21st AIAA/CEAS Aeroacoustics Conference, AIAA 2015-2205 paper, Dallas, TX, 2015, http://dx.doi.org/10.2514/6.2015-2205.
[50] M. Pestana, A. Pereira, E. Salze, J. Thisse, M. Sanjose, E. Jondeau, P. Souchotte, M. Roger, S. Moreau, J. Regnard, M. Gruber, Aeroacoustics of an axial ducted low mach-number stage: numerical and experimental investigation, in: 23rd AIAA/CEAS Aeroacoustics Conference, in: AIAA Paper 2017-3215, American Institute of Aeronautics and Astronautics, 2017.
[51] F. Czwielong, F. Kromer, S. Becker, Experimental investigations of the sound emissions of axial fans under the influence of suction-side exchangers, in: 25th AIAA/CEAS Aeroacoustics Conference, 2019, p. 2168.
[52] E. Canepa, A. Cattanei, F.M. Zecchin, Scaling properties of the aerodynamic noise generated by low-speed fans, J. Sound Vib. 408 (2017) 291–313, http://dx.doi.org/10.1016/j.jsv.2017.07.031.
[53] A. Zarri, J. Christophe, S. Moreau, C. Schram, Influence of swept blades on low-order acoustic prediction for axial fans, Acoustics 2 (4) (2020) 812–832, http://dx.doi.org/10.3390/acoustics2040046.
[54] M. Sanjosé, S. Moreau, Fast and accurate analytical modeling of broadband noise for a low-speed fan, J. Acoust. Soc. Am. 143 (5) (2018) 3103–3113.
[55] G. Herold, B11, 2017, https://www.b-tu.de/fg-akustik/lehre/aktuelles/arraybenchmark.
[56] S. Moreau, M. Roger, Effect of airfoil aerodynamic loading on trailing-edge noise sources, AIAA J. 43 (1) (2005) 41–52.
[57] J. Christophe, J. Anthoine, S. Moreau, Trailing edge noise of a controlled-diffusion airfoil at moderate and high angle of attack, in: 15th AIAA/CEAS Aeroacoustics Conference, in: AIAA Paper 2009–3196, 2009.
[58] R.E. Longhouse, Noise separation and design considerations for low tip-speed and axial-flow fans, J. Sound Vib. 48 (4) (1976) 461–474.